Exploring Sequential Snapping Bifurcation through Tunable Energy Landscape

Ke Huang[1], Jiaying Zhang[1,*], Weicheng Huang[2], Qingyun Wang[1], Alexander D. Shaw[3] and Michael I. Friswell[3]

[1] School of Aeronautic Science and Engineering, Beihang University, Beijing 100191, China
[2] School of Engineering, Newcastle University, Newcastle upon Tyne NE1 7RU, United Kingdom
[3] Department of Aerospace Engineering, Swansea University, Swansea SA1 8EN, United Kingdom

ABSTRACT. Bifurcation, which alters the number and stability of equilibria in multistable systems, is the primary mechanism governing the formation of elastic sequential snap-through instabilities. However, to date, there is no general understanding of the multistable energy landscape organized by bifurcations underlying snap-through. Here, we conduct a theoretical, numerical and experimental analysis of serial bistable planar curved beams widely proposed in recent literature, developing numerical algorithms and experimental schemes to explore the bifurcation structures within the energy landscape. Such systems provide sufficient physical transparency due to their low dimension and clear interaction, making them ideal for analysing bifurcation structures. Two types of elastic sequential snap-through instabilities are discovered: competition-induced phase transitions triggered by limit forces (switching fields) between units and unit phase transitions triggered by the equivalent stiffness of system variables within each unit. Our method proposes a general tunable snap-through paths design strategy in multistable systems, which can be extended to broader systems with interacting units. Importantly, through tuning stiffness properties and the limit force perturbations, custom-designed saddle-node bifurcation pairs and traverse stable paths can be achieved, thus providing universal design rules for elastic sequential transitions.

I. INTRODUCTION

The complex energy competition mechanisms in frustrated media, such as crumpled sheets and metamaterials, lead to the formation of a rugged energy landscape in multistable systems [1-4], resulting in complex and highly nontrivial transition paths [5-7]. Information can be stored and transmitted within the geometric structures [8], enabling universal combinatorial logic [9,10] and sequential information processing [11,12]. Due to the widespread presence of bifurcations in the potential energy landscape of multistable systems [13,14], snap-through occurs when a stable branch becomes unstable or vanishes as control parameters vary, causing the system to abruptly transition [15,16]. Therefore, analyzing the bifurcation structures that organize the energy landscape allows exploration of phenomena across scales, including jagged responses, jumps, and avalanches, from alloy phase transitions and macromolecular materials [17] at the microscopic level to crumpled sheets [18] and snapping metamaterials [19,20] at the macroscopic level.

Exploratory studies of multistable systems often examine hysteresis and memory effects via experiments and simulations [11,18,21]. Many multistable systems can be decomposed into interacting bistable units based on structural or response characteristics, such as hysterons [11] and bistable nearest-neighbor springs [2,3]. Studies attribute complex phenomena to the intricate interactions between bistable units, but micro-mechanisms of interactions among bistable units in frustrated media are often neglected. For multistable mechanical metamaterials [22] with limited bistable units, applying bifurcation theory [23] as a "microscope" to amplify local responses and examine inter-unit competition can reveal interaction mechanisms and enable targeted snapping pathways.

Although analytical and numerical studies have clarified the phase-transition mechanisms within bistable chains, the bifurcation mechanisms underlying competition between units are less explored. Here, we investigate the snap-through induced by elastic instability in multistable systems composed of bistable units. The bistable units studied here do not exhibit discontinuous snap-through, i.e., no hysteresis, under displacement-controlled loading [24,25]. The coupling relationships between bistable units introduce energy competition mechanisms that lead to the destabilization or disappearance of stable branches in the bifurcation structure, causing the system to undergo violent transitions.

*Contact author: jiaying.zhang@buaa.edu.cn

II. ANALYSIS OF BISTABLE UNITS

A. Theoretical model of bistable beams

Bistable beams, commonly used in the construction of multistable metamaterials, are employed here as bistable units [19,20]. By adjusting the beam geometric parameters, precise control over the mechanical properties can be achieved [11,25-27], and coupling between bistable units is realized through a serial and parallel arrangement [28]. Common structures of bistable beams are illustrated in Figs. 1(a) and 1(b). The bistable beams studied here are centrally clamped, suppressing anti-symmetric transition modes. Bistable beams can be categorized into pre-buckled beams and pre-shaped beams, with the main difference being the symmetry-related mechanical characteristics due to initial structural symmetry. The resulting symmetry and symmetry-broken mechanical responses are shown in Figs. 1(c) and 1(d).

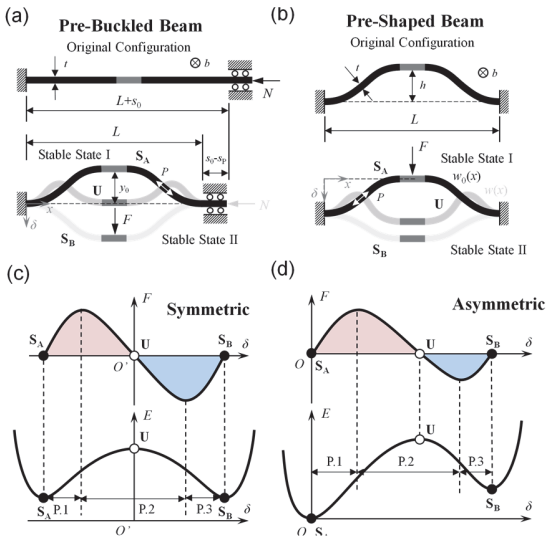

FIG 1. Bistable beam models. (a) A straight beam (length $L + s_0$) is compressed by an axial load N to reach the first buckling mode. The compression distance is $s_0 - s_P$, with s_P being the axial deformation due to the axial internal force P. (b) A curved beam with initial shape $w_0(x) = h/2[1 - \cos(2\pi x/L)]$. Force-displacement ($F$- δ) and potential energy curves illustrating (c) symmetric and (d) asymmetric behavior.

Mechanical properties of bistable beams are derived by the minimum potential energy principle [25,31], a more detailed derivation is given in the Supplemental Material[30], Sec. S1. The force-displacement (F-δ) response of buckled beams is expressed as a piecewise function. When $2\pi \le \eta L < 4\pi$:

$$F(\eta) = -\frac{EI}{2L^3}\sqrt{[s_0 - s_P]L}\left[3 - \frac{3}{\eta L}\tan\left(\frac{\eta L}{4}\right) + \tan^2\left(\frac{\eta L}{4}\right)\right]^{-1/2} \quad (1)$$

$$\delta(\eta) = -\frac{L^3}{EI(\eta L)^2}F(\eta)\left[\frac{1}{4} - \frac{1}{\eta L}\tan\left(\frac{\eta L}{4}\right)\right] \quad (2)$$

where $s_P = (\eta L)^2 I/(LS)$, with η being the free parameter of the parameterized equation. L, EI and S are the length, bending stiffness and cross-sectional area of the beam, respectively.

When $\eta L \ge 4\pi$:

$$F(\delta) = -\frac{64\pi^2 EI}{L^3}\delta \quad (3)$$

Similarly, the force-displacement response of the pre-curved beam is also given by piecewise functions. The first-order mode's generalized force F_1 and displacement are given by

$$F_1(\delta) = 3\pi^4\frac{EIQ^2}{h^2L^3}\delta\left(\delta^2 - 3h\delta + 2h^2 + \frac{4h^2}{3Q^2}\right) \quad (4)$$

where $Q = h/t$.

The explicit expressions for the generalized force of the third-order symmetric mode F_3 is given by

$$F_3(\delta) = 2\pi^4\frac{EI}{L^3}(4h - 3\delta) \quad (5)$$

The force-displacement characteristics of the pre-curved beam are determined by the numerical minimum values of Eqs.(4) and (5).

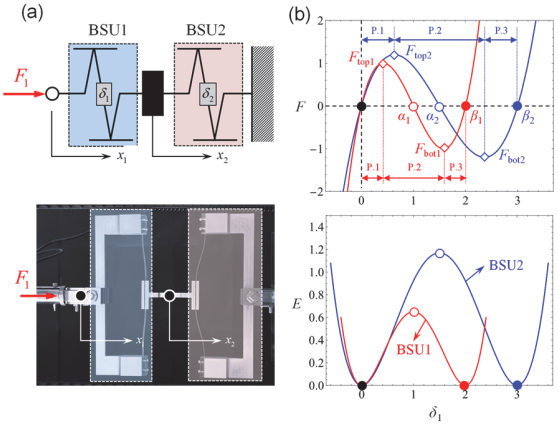

FIG 2. Classical two-unit model. (a) Diagram and experimental setup of two bi-stable units in series, with δ_i as the displacement of the i-th unit, absolute displacement x_1 (end-point) and x_2 (mid-point); F_{topi} and F_{boti} represent the maximum and minimum limit force of the i-th bistable unit, respectively. (b) Force-displacemen and potential energy curves for BSU1 (red) and BSU2 (blue); filled circles: energy minima, empty circles: maxima.

3D printing techniques are used to create these beams to demonstrate bistable characteristics (Movie S1[30]).The force-displacement behavior of bistable clamped beam units has three stages: positive stiffness in stages P.1 and P.3 and negative stiffness in stage P.2 [Figs. 1(c) and 1(d)]. Each stage has one equilibrium point: stable ($\mathbf{S_A}$, $\mathbf{S_B}$) in positive stiffness regions and

*Contact author: jiaying.zhang@buaa.edu.cn

unstable (**U**) in the negative stiffness region. The bistable unit turns to P.2 after crossing the potential barrier at **U**.

B. Simplified bistable model

A simplified expression of bistable behavior [32] is introduced to concisely capture complex properties, as shown in the following equation

$$F_i(\delta_i) = K_i\delta_i(\delta_i - \alpha_i)(\delta_i - \beta_i) \quad (6)$$

where α_i and β_i denote the unstable and the second stable equilibrium positions of the i-th bistable unit (BSU), respectively, and F_i, δ_i, and K_i are the force, displacement, and a proportionality constant of the i-th BSU. The force-displacement response of the bistable beams, as derived from Eqs. (1)–(5), is fitted using a simplified expression [Eq.(6)] via *MATLAB*'s Curve Fitting Toolbox. The efficacy of this simplified expression in reproducing the essential bistable characteristics of the beam is thoroughly examined in the Supplemental Material [30], Sec. S2.

III. BIFURCATION ANALYSIS IN MULTISTABLE SYSTEMS

A. Classical two-unit model

The force-displacement curves of multistable systems assembled by bistable units are complex. Thus, we analyze a classical two-unit model [Fig.2(a)]. The two-unit model captures recurring transitions seen in larger networks of bistable units, while retaining sufficient physical transparency [29]. One end of BSU2 is fixed, while the other end is serially connected to BSU1 at the mid-point. x_2 is the displacement of the mid-point. An end-point displacement load x_1 is applied on the opposite side of BSU1. Despite its simplicity, the two-unit model reveals transition pathways between metastable states from complex couplings in larger systems [5]. This simplification aids in identifying bifurcation structures and analyzing underlying mechanisms. We will analyze and discuss more complex and larger networks of bistable units in Section V.

Each bistable unit is modeled by a cubic polynomial [Eq.(6)], so that its potential energy $E(x) = \int_0^x F(\delta)\, d\delta$ becomes a quartic polynomial. The total potential energy is $E_{\text{tot}}(x_2, x_1) = E_1(x_1 - x_2) + E_2(x_2)$. The relationship between the two units is defined by the symmetry parameters $r_i = \alpha_i/\beta_i\,(i = 1,2)$, $\xi = F_{\text{top2}}/F_{\text{top1}}$ and $\varphi = \alpha_2/\alpha_1$, with $\alpha_1 = 1$ for subsequent analysis. In Fig. 2(b) and Fig. 3, $r_1 = r_2 = 2$, $\xi = 1.2$, $\varphi = 1.5$. We investigate stable state transition under overdamped, quasi-static loading for a two-unit model. The potential energy landscape is shown in Fig. 3(a), which features four potential energy minima (E_j), four potential energy saddle points (S_k), and one potential energy maximum (M) of the energy landscape.

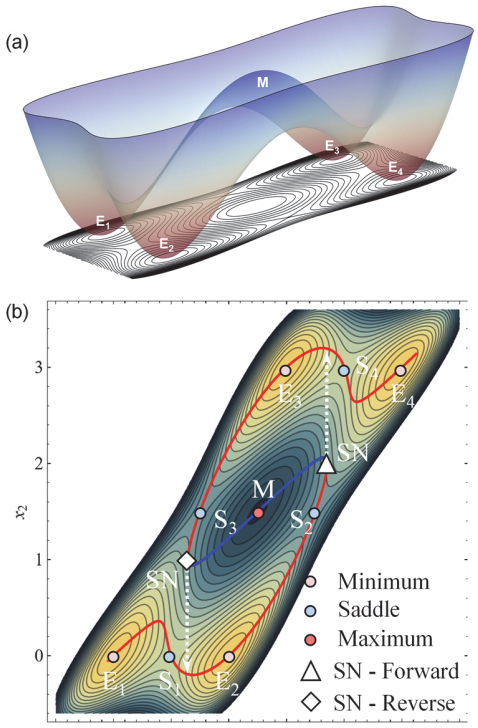

FIG 3. Multistable energy landscape. (a) Illustration of an energy landscape of a 2D energy surface. (b) Potential energy contour and transition pathway. The red and blue lines denote the stable and unstable parts of the pathway, respectively, for fixed x_1. Underlying inset below shows bifurcation criteria of the cusp catastrophe model (E: Equilibrium, S: Saddle, M: Maxima, SN: Saddle-Node bifurcation).

B. Bifurcation analysis

Let x_1 be the bifurcation parameter, then stable configurations are found by solving the equilibrium equation $dE_{\text{tot}}/dx_2 = 0$ to obtain x_2 as the state parameter via the *Solve* function in *Mathematica* within the real number range. Based on simple linear stability analysis, the stability of the corresponding equilibrium configurations can be assessed by the second derivative of the energy $\partial^2 E_{\text{tot}}/\partial x_2^2$. The sign of d^2E_{tot}/dx_2^2 determines the stability of the system: a positive value indicates stability, while a negative value indicates instability. The transition pathways are represented in the bifurcation diagram with colors (red/blue) to indicate stability (stable/unstable) as shown in Fig.3(b). Singular points occur where $d^2E_{\text{tot}}/dx_2^2 = 0$, which are saddle-node bifurcations (SN, $dx_2/dx_1 = \infty$) causing structural topology changes. These appear as intersections and limit points of stable and unstable equilibrium pathways,

*Contact author: jiaying.zhang@buaa.edu.cn

representing symmetry-broken bifurcations due to parameter differences between the two units [23]. To facilitate understanding of the bifurcation and snap-through phenomena occurring during the system's transition, the transformation of a graceful pitchfork bifurcation into a violent saddle-node bifurcation due to symmetry breaking in a single degree-of-freedom system is detailed in the Supplemental Material [30], Sec. S3A.

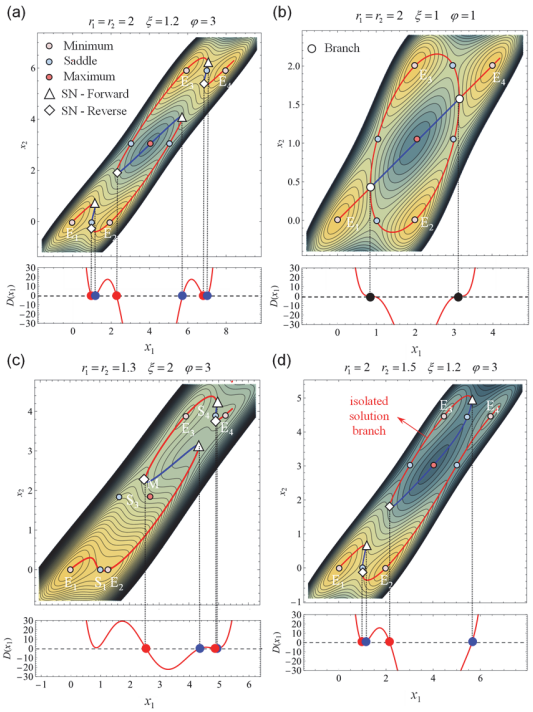

FIG 4. Potential energy contour and transition pathways for different unit parameters, as indicated in each subplot title (a-d). The red and blue lines denote the stable and unstable parts of the pathway, respectively, for fixed x_1. Underlying inset below shows bifurcation criteria of the cusp catastrophe model (E: Equilibrium, S: Saddle, M: Maxima).

The number of accessible stable states can lead to various scenarios. In the first case, as shown in Fig. 4(b), the bistable unit characteristics are identical, and no SN bifurcation occurs due to perfect symmetry; instead, a supercritical pitchfork bifurcation (PF) occurs, akin to buckling Euler beams making stable state transitions dependent on local perturbations at the bifurcation point.

When all four stable states are accessible, treating bifurcation points connected by unstable branches as pairs reveals three scenarios in the stable equilibrium pathways, as shown in Figs. 3(b), 4(c), and 4(a), with one, two, or three pairs as parameters vary. Diagrams of stable branches show two types of bifurcations: those occurring before the saddle point and those jumping past or occurring after it, classified herein as SN1 and SN2 bifurcations respectively.

The cusp catastrophe is a standard elementary catastrophe model [33], illustrated in Fig. S5.1 with its state-bifurcation parameter space. Using the cusp catastrophe model's bifurcation set yields a sixth-order discriminant

$$D(x_1) = 8U'(x_1)^3 + 27V'(x_1)^2 = \sum_{i=0}^{6} a_i x_1^i \qquad (7)$$

where the discriminant's coefficients a_i are constants determined by the mechanical properties of the element, and $U'(x_1), V'(x_1)$ are polynomials in x_1, the expression is rearranged into the canonical form of the bifurcation set for the cusp catastrophe model. The detailed expressions are given in the Supplemental Material[30], Sec. S5.

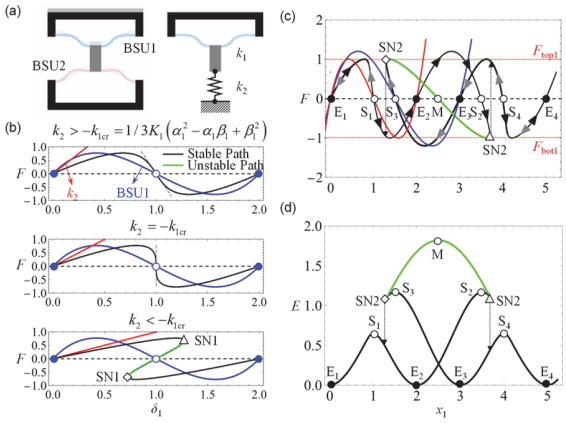

FIG 5. Mechanism analysis of two types of SN bifurcation. (a) A linear spring represents the positive stiffness of one unit for SN1 analysis, with BSU2 modeled by a spring of stiffness k_2. (b) Effect of reduced equivalent spring stiffness on the unit's force-displacement characteristics. As k_2 decreases, the unit's negative stiffness range narrows, reaching critical stiffness $-k_{1cr}$ as negative stiffness approaches infinity. k_{1cr} is the maximum negative stiffness of BSU1. When $k_2<-k_{1cr}$, a pair of SN1 bifurcations occurs. (c) and (d) The F–x_1 and E–x_1 curves using parameters from Fig.1(c). Black arrows indicate positive loading; gray arrows indicate negative loading. The limit force of BSU1 (red line) is lower than that of BSU2 (blue line). This difference induces SN2, which occurs when BSU1 reaches another stable state, and subsequently, BSU2 reaches BSU1's limit force of BSU1(red dash line).

When $D > 0$, the system has three fixed points. When $D < 0$, it has one. Thus, when $D = 0$, the system undergoes a SN bifurcation with $dD(x_1)/dx_1 \neq 0$ or a PF/cusp bifurcation with $dD(x_1)/dx_1 = 0$. The

*Contact author: jiaying.zhang@buaa.edu.cn

underlying insets in Fig.4 show the bifurcation criteria of the cusp catastrophe model [Eq.(7)], accurately identifying the critical bifurcation points along the classical two-unit model's transition pathway and direction of the snap-through. The cusp catastrophe model indicates that the structure can exhibit up to six bifurcation points. The slope sign at the zeros of the criterion denotes bifurcation occurrence on the upper or lower cusp catastrophe equilibrium manifold sheets. Analysis shows that in multistable systems with serial bistable units, only one unit becomes unstable during snap-through [2,3]. Therefore, when one unit is in stage P.2, units in stages P.1 or P.3 can be modeled as springs. For qualitative analysis, another bistable unit is simplified as a linear spring, shown in Fig. 5(a), connecting bistable units. When linear spring stiffness k_2 in the first and third stages is less than the maximum absolute negative stiffness of the second stage $-k_{1cr}$, the structure undergoes a SN1. Thus, SN1 is related to the stiffness characteristics of bistable units. For the detailed derivation of $-k_{1cr}$, refer to the Supplemental Material [30], Sec. S4. This simplified model demonstrates that once an SN1 occurs, the unstable equilibrium pathway passes through the saddle point, and a conventional loading cycle will jump past it.

The SN1-type bifurcation-induced snap-through is the key mechanism to the jagged force-displacement response [17]. Previous work [17] proposed that all bistable units can be decomposed into a spring and an ideal bistable unit, with each phase transition involving only one unit under the over-damped assumption. Thus, non-transitioning units can be treated as a single equivalent spring connected with the transitioning unit. This approach maps the system to the model in Fig. 5(a). However, when the equivalent spring stiffness is small enough to induce SN1 bifurcations, the resulting snap-through produces regularly spaced jagged response patterns (Fig.17). Such stiffness-induced bifurcations also occur in muscle mechanics [34] and memory formation in disordered materials [35].

SN2 bifurcations are related to the prior known limit forces or switching fields of bistable units. As shown in Fig. 5(c), during loading, one bistable unit reaches its stage P.2. Further loading causes the bistable unit to reach the limit force in the opposite direction of the loading direction, inducing a bifurcation similar to that occurring under force loading. Inspired by the directionally buckled beams with imperfections [12] and the rapid shape transitions of elastic buckled strips driven by broken symmetries at the boundaries [14,15], the difference in limit forces between units can be viewed as a perturbation to the identical unit system. Near the pitchfork bifurcation point, the normal form of the equilibrium equation can be obtained, revealing that the introduction of the perturbation corresponds to the addition of asymmetric parameters to the symmetric pitchfork bifurcation system, leading to the formation of a pair of SN2 bifurcations at the limit points of the detached branches induced by the broken symmetries of the pitchfork bifurcation, as shown in Fig.6(a). The theoretical demonstration of imperfect pitchfork bifurcations induced by initial asymmetry introduced through structural parameters is provided in the Supplemental Material [30], Sec. S3B.

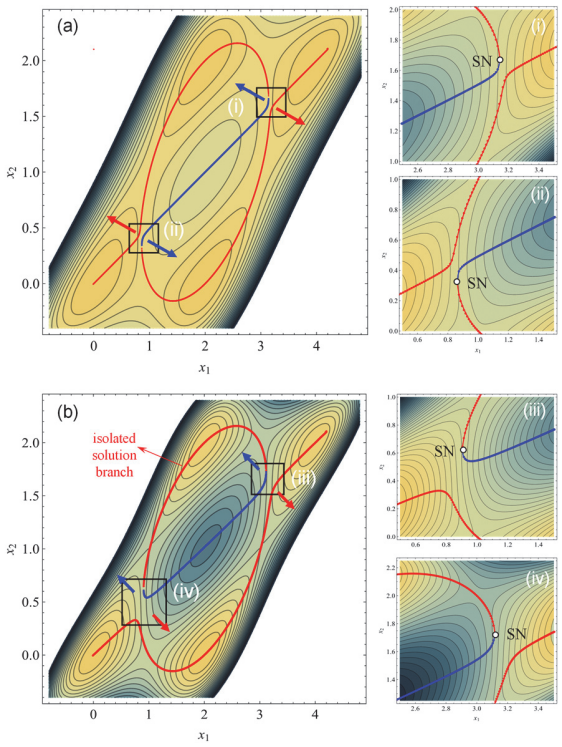

FIG 6. The imperfect pitchfork bifurcations. Initial asymmetry being introduced into the structural parameters of the system, which originally displays a symmetric pitchfork bifurcation in Fig. 4(b). (a) $K_1 = K_2 + \Delta K = 1, \Delta K = 0.01, \alpha_1 = \alpha_2 = 1, \beta_1 = \beta_2 = 2$. (b) $F_{\text{top1}} = F_{\text{top2}} - \Delta F = 1, F_{\text{bot1}} = F_{\text{bot2}} + \Delta F = 1, \Delta F = 0.05$. Equilibrium pathway for fixed x_1 displacement (red: stable, blue: unstable) with two SN bifurcations. (i-iv) Zoomed-in views of the SN bifurcations.

In multistable systems with asymmetric units, certain stable states are inaccessible, as shown in Fig. 4(d). In the potential energy landscape, inaccessible states appear as isolated branches, with stable and unstable equilibrium pathways forming closed loops joined by SN bifurcations, making it impossible to reach these isolated branches from the initial configuration under quasi-static loading [Fig.6(b)]. When the sequence of maximum forces and minimum forces is inconsistent ($|F_{\text{top}i}| < |F_{\text{top}j}|, |F_{\text{bot}i}| >$

*Contact author: jiaying.zhang@buaa.edu.cn

$|F_{\mathrm{bot}j}|$), the isolated branch will form a minimal energy path between nearby saddle points, maxima, and inaccessible stable states, governed by the "minimal barrier" strategy [3] and branch detachment under symmetry-breaking organization. This phenomenon is widely observed in Preisach t-graphs, where inaccessible stable states form parent graphs of hysteron transition pathways [5,11].

IV. EXPERIMENTAL CONTINUATION OF UNSTABLE EQUILIBRIUM MANIFOLDS

A. Fabrication and experimental setup

Based on the analysis, inaccessible unstable paths exist in the equilibrium pathway of multistable systems. Using the experimental continuation method related to shape control [36], the unstable equilibrium pathways are tracked. Figure 7 provides detailed descriptions of the basic concept of shape control and the experimental setup. As shown in Figs. 7(b) and 7(c), an additional mid-point probe connected to a force sensor explored the unstable equilibrium pathway under end-point displacement x_1 constraint. End displacement load was incrementally increased ($\Delta x_1 = 1\mathrm{mm}$), with the mid-point displacement x_2 adjusted along a linear guide at each step (Movie S2 [30]). The experimental details are described in Supplemental Material[30] Sec. S7.

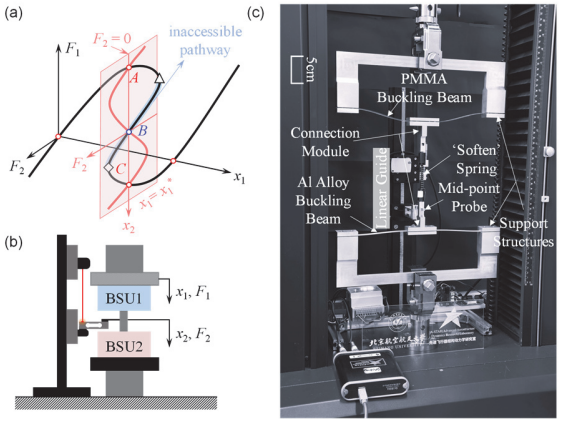

FIG 7. Experimental setup. (a) Basic principle of the shape control. SN bifurcations create hysteresis, resulting in inaccessible pathways within the hysteresis loop. Using the mid-point probe from stable states A/C, this path is accessible at state B when $x_1 = x_1^*$. F_1 and F_2 represent the forces at the end-point and mid-point, respectively. (b) Coordinate and force definitions in the schematic diagram. The red line indicates the displacement sensor's laser. (c) Physical setup for the multistable modulus experiment.

B. Displacement load-controlled testing

Aluminum alloy and PMMA (Polymethyl Methacrylate) buckled beam samples are chosen to avoid viscoelastic effects in flexible silicone [37]. Aluminum alloy beams were CNC-machined, and PMMA beams were laser-cut. Both beam types were manually compressed to induce buckling and fastened with screws to CNC-machined aluminum alloy supports. The buckling beams were connected with an elastic module. The geometric parameters, material properties and sample fabrications are detailed in Supplemental Material[30] Sec. S6.

The force-displacement responses of the bistable units and the multistable modulus under displacement-controlled loading are detailed in the experimental setups illustrated in Figs. S7.1(a), S7.1(b) and 8(a), respectively. The fitting accuracy of the simplified expression [Eq. (6)] in capturing the mechanical response of the bistable units was evaluated, as shown in Figs. 8(b) and 8(c). For the aluminum alloy buckling beam and the PMMA buckling beam equipped with a "softening" spring of appropriately selected stiffness, the simplified expression accurately captures the force-displacement behavior of the bistable units.

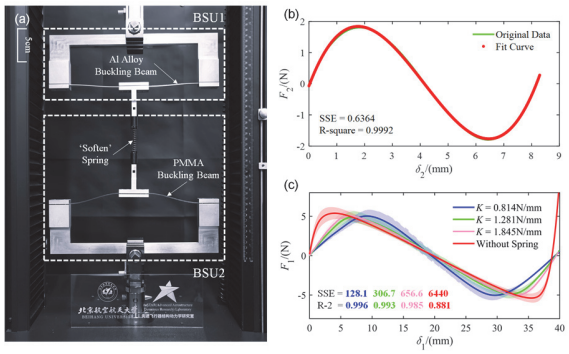

FIG 8. Experimental scheme and results. (a) The multistable modulus with "softening" springs. The configurations of BSU1 and BSU2 are delineated by the white dashed boxes. Experimental results for: (b) BSU1—Al alloy buckling beam; (c) BSU2—PMMA buckling beam with "softening" springs. The goodness of fit for the simplified expression [Eq. (6)] is evaluated using SSE (sum of squares due to error) and R-square, where an SSE close to zero and an R-square near one indicate a high-quality fit.

The response of the multistable modulus both with and without the "softening" spring (i.e., with rigid connections) under displacement-controlled loading is presented in Figs. 9(a) and 9(b), respectively. Snap-through is accompanied by a decaying structural oscillation, caused by the sudden release of energy at the transition; the oscillation is progressively damped

*Contact author: jiaying.zhang@buaa.edu.cn

by structural dissipation. In Fig. 9(b), the small step-like response observed in the negative-stiffness region for x_1 = 23-35 mm arises from the stick–slip behavior of the 'softening' spring (Fig. S6.2) with the slide guide. Corresponding experimental demonstrations are provided in Movies S3 and S4 [30].

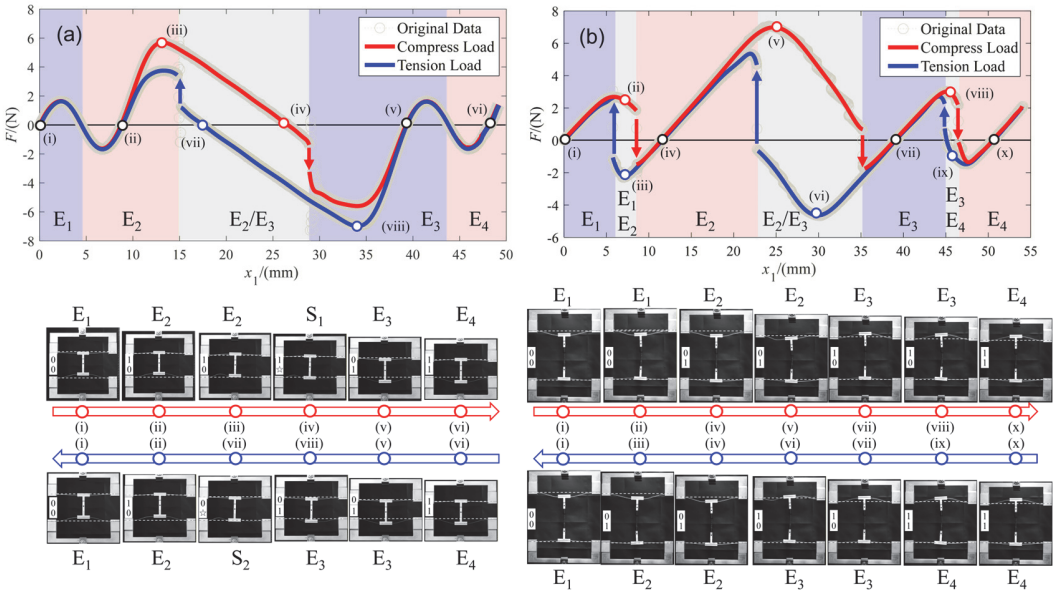

FIG 9. Multistable modulus mechanical response without mid-point probe support. (a) without and (b) with 'softening' spring and displacement control for x_1. F represents the reaction force measured after applying the displacement load x_1. The bottom row of insets shows photographs of the experimental module during the state-transition process. White dashed lines mark the saddle points of each unit, and a bistable beam crossing a white dashed line indicates a state transition of that unit (E: equilibrium, S: saddle; subscripts distinguish different states).

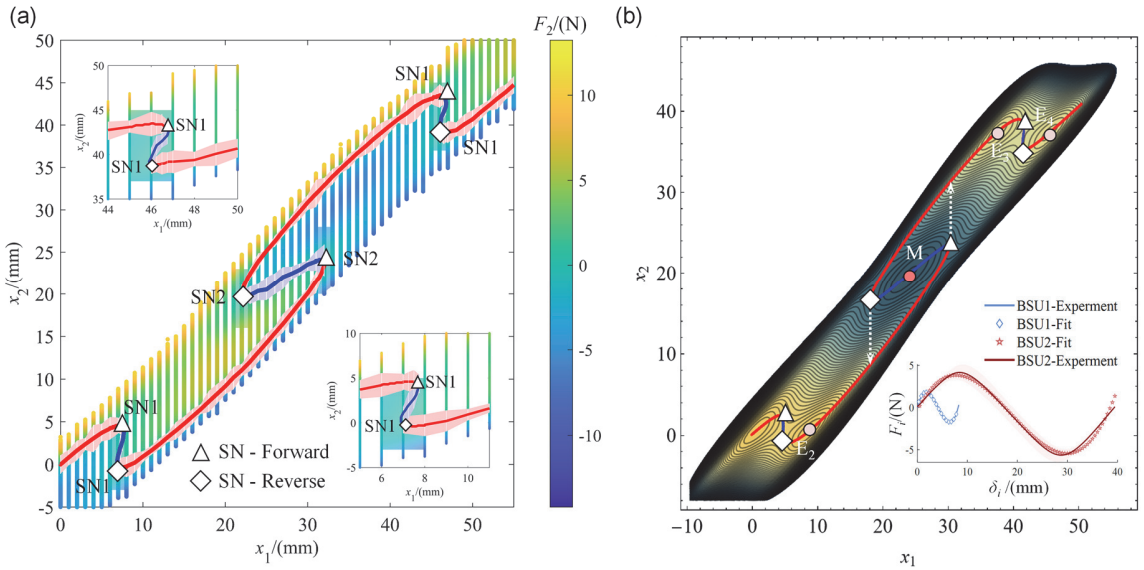

FIG 10. Comparison of experimental and theoretical model results. (a) End-point and mid-point scan results. Data for x_1, x_2, and F_2 are shown in 3D, converted to a top-down view. Red and blue lines represent stable and unstable equilibrium states at $F_2 = 0$, and the colored areas represent one standard deviation of x_2. Surface interpolation in specific intervals locates SN bifurcations (Supplemental Material[30] Sec. S7). (b) Using the potential energy landscape model, the transition pathway is identified after fitting mechanical properties with a cubic polynomial. The inset shows experimental results of unit mechanical properties compared with polynomial fitting (Supplemental Material [30] Sec. S7).

*Contact author: jiaying.zhang@buaa.edu.cn

In experiments with rigid connections, only SN2 bifurcations are observed [point(iii) and (viii) in Fig.9(a)] (Movie S3[30]). However, by incorporating a serially connected "softened spring" with moderate stiffness, the unit's positive stiffness can be adjusted without affecting the limit force [Fig.8(c)], thereby satisfying the conditions for both SN bifurcations as predicted by the theoretical analysis. As previously discussed, to facilitate SN1 bifurcations, the BSU with the larger limit force must also have relatively smaller positive stiffness in stages P.1 and P.3 compared to the negative stiffness in stage P.2 of another BSU [Fig. 5(b)]. The beam geometry and spring stiffness are then chosen to ensure the occurrence of both bifurcations. As a result, an evident snap-through event induced by an SN1-type bifurcation is observed in Fig. 9(b) (Movie S4[30]).

The equilibrium pathway is unstable under displacement loading but is stabilized by the mid-point probe, as shown in Fig.9. Introducing an additional mid-point probe to control a second degree of freedom, with displacement load fixed, allows scanning of zero-force positions between stable configurations to identify unstable equilibrium pathways.

C. Experimental continuation testing

Limit points of the equilibrium pathway from experimental continuation reveals bifurcations in multistable systems with serial-connected bistable elements. Figure 10 shows system transition with three pairs of SN bifurcations induced by adding spring units. Despite nonlinear systems' sensitivity to initial conditions, theoretical and experimental results align qualitatively and quantitatively, validating the feasibility of analyzing multistable systems using potential energy landscapes and bifurcation theory. Here, a general tenable snap-through paths design strategy can be achieved through tuning stiffness properties and the limit force perturbations for elastic sequential transitions.

V. BEYOND TWO-UNIT SYSTEMS

A. Typical state transition graphs in the two-unit system

When the sequence of the maximum force F_{top} and the minimum force F_{bot} is consistent between the two units in the two-unit system, their transition pathways can differ significantly. This difference manifests in the relative position of the critical snapping load (field) within the bifurcation parameter space with respect to the different stable states. In Figs. 4(a) and 3(b), the two units follow distinct transition pathways. From the state transition graph in Fig. 11, the key difference is the position of snapping under forward and reverse loading with respect to E_3 and E_2. If, under forward loading, snapping occurs before reaching E_3, the system transitions from E_2 to E_3 [Fig. 11(a)], as also seen in Fig. 9. Otherwise, E_3 cannot be reached from E_2 under monotonic loading, and the transition between these two states must pass through E_1 and E_4 [Fig. 11(b)]. Previous studies refer to the transition from E_2 to E_3, which involves switching the stable states of both units, as an "avalanche" [5]. An isolated solution branch can also render some stable states unreachable, such as E_3 in Fig. 11(c).

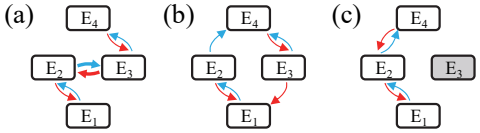

FIG 11. Typical possible state transition pathways in the two-unit series system. (a) Case corresponding to Fig. 4(a) and the experimental results in Fig. 9. (b) Case corresponding to Fig. 3(b). (c) Case corresponding to Fig. 4(d). Blue arrows indicate forward loading, and red arrows indicate reverse loading. Thin arrows denote switching of the stable state of a single unit, while thick arrows denote avalanche events.

B. Equilibrium equations and stability analysis of the *N*-unit series system

For a system of N bistable units in series, we denote the absolute displacement of each unit by x_i. Summing over the potential energy $E_i(x_i - x_{i+1})$ of all BSUs, the total energy of the system can then be written as

$$E_{\text{tot}}(x_1, x_2, \ldots, x_{n+1}) = \sum_{i=1}^{n} E_i(x_i - x_{i+1}) \qquad (8)$$

Here x_1 is the displacement load, and x_{N+1} corresponds to the fixed end, i.e., $x_{N+1} = 0$.

*Contact author: jiaying.zhang@buaa.edu.cn

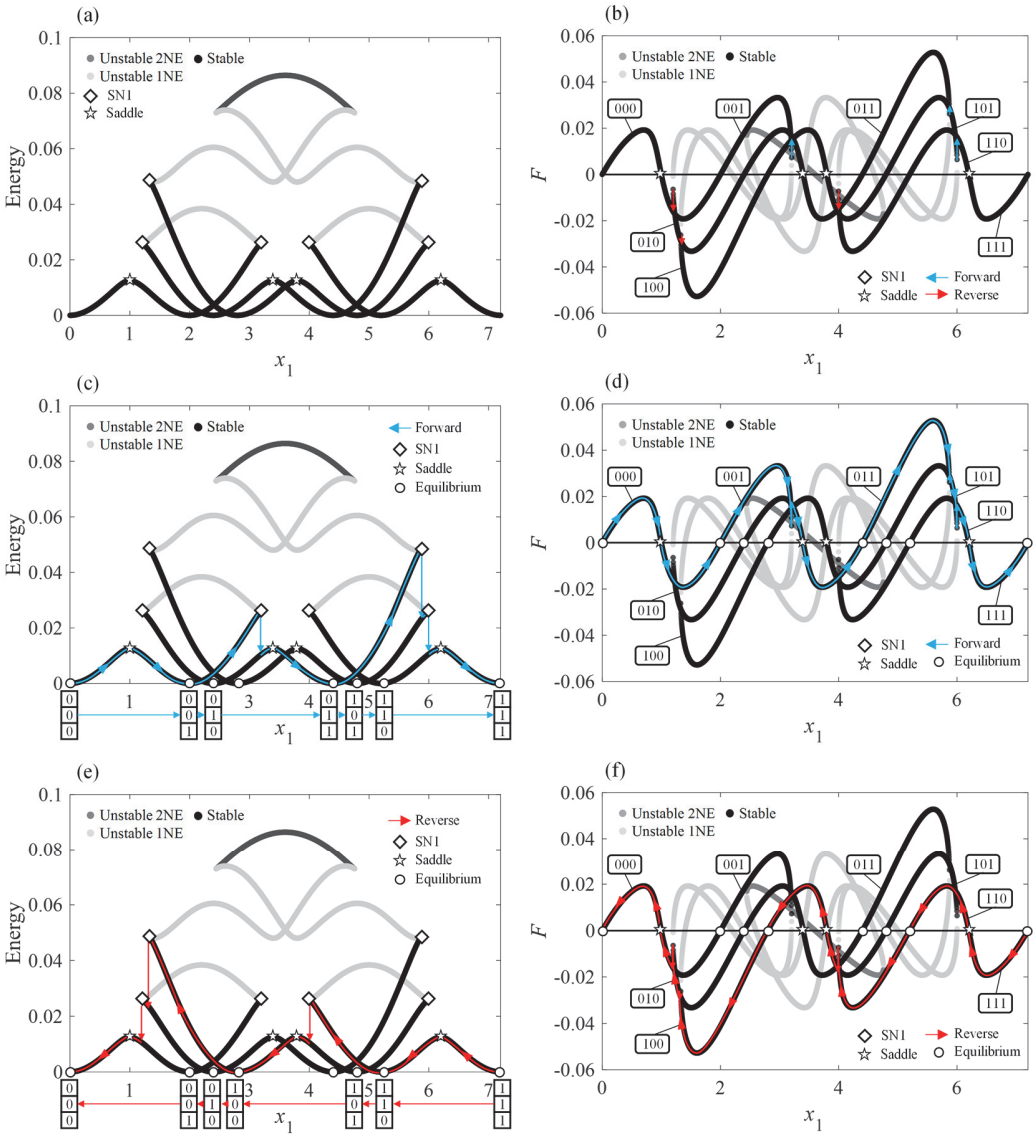

FIG. 12. Transition pathways of the three-unit series system (Set 1). (a) Energy landscape of all equilibrium states of the system. (b) Force-displacement relation of all equilibrium states. (c),(d) Highlighted blue curves denote the forward-loading state transition pathway in the energy landscape and in the force-displacement response, respectively. (e),(f) Highlighted red curves denote the reverse-loading state transition pathway in the energy landscape and in the force-displacement response, respectively.

The equilibrium equations of the system are given by

$$\boldsymbol{F} = \left[\frac{\partial E_{\text{tot}}}{\partial x_i}\right] = 0 \ \ (i = 2,3,\dots,n) \tag{9}$$

The equilibrium solutions in this section, obtained by solving Eq.(8), are computed using the Solve function in *Mathematica* within the real number range. To assess the stability of each equilibrium solution, we further differentiate the equilibrium equations and obtain the Hessian matrix $\boldsymbol{H}$ of the total energy as

$$\boldsymbol{H} = \left[\frac{\partial^2 E_{\text{tot}}}{\partial x_i \partial x_j}\right] = 0 \ \ (i,j = 2,3,\dots,n) \tag{10}$$

The stability of each equilibrium point is determined by the signs of the eigenvalues of the Hessian matrix evaluated at that point. If all eigenvalues are positive, the equilibrium is stable. The presence of any negative eigenvalue implies that the equilibrium point is unstable. The subsequent equilibrium solutions are then grouped by the number of negative eigenvalues, which gives the Morse index of each equilibrium [1].

*Contact author: jiaying.zhang@buaa.edu.cn

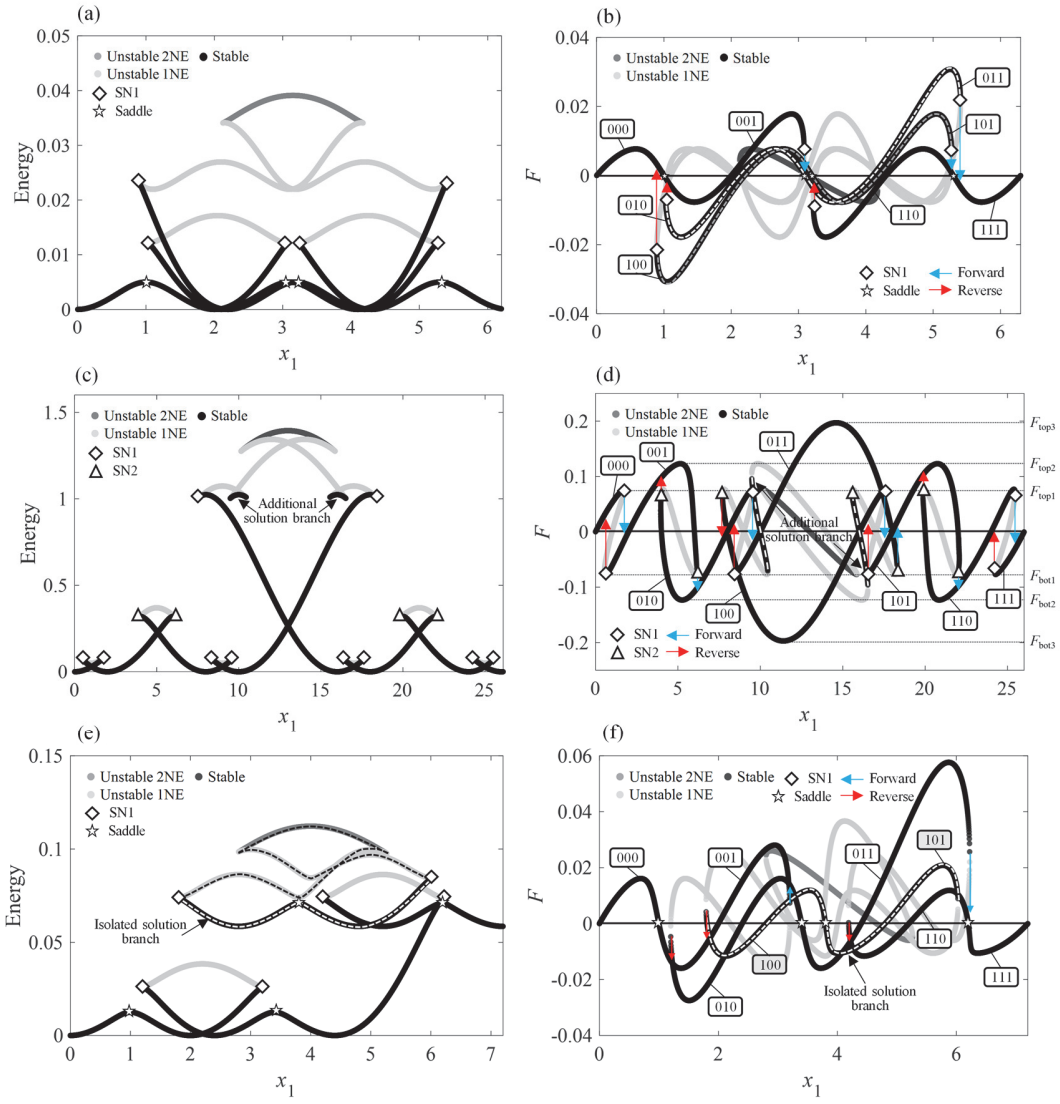

FIG. 13. Transition pathways of the three-unit series system with parameter (a-b) set 2, (c-d) set 3, (e-f) set 4 in Table I. (a,c,e) Energy landscape, (b,d,f) Force–displacement relation.

C. Three-unit series system

We label the stable state with zero displacement of each bistable unit as $s_i = 0$, and the other stable state as $s_i = 1$. The overall state is written as $\mathbf{s} = (s_3, s_2, s_1)$, where the subscript of s_i indicates the unit index.

TABLE I. The Data Used in Section V.C.

Set	K(BSU1/2/3)	α(BSU1/2/3)	β(BSU1/2/3)
1	0.05/0.05/0.05	1.0/1.2/1.4	2.0/2.4/2.8
2	0.02/0.04/0.06	1.0/1.05/1.1	2.0/2.1/2.2
3	0.2/0.005/0.001	1.0/4.0/8.0	2.0/8.0/16.0
4	0.04/0.05/0.04	1.0/1.2/1.8	2.0/2.4/2.8

Table I lists the parameters of the three-unit series system used in this section. In Figs.12 and 13, several branches involve multiple states. When branches corresponding to different states connect continuously, we separate them by saddle points, which are marked by star symbols in the figures. If the stable force–displacement curve of a given state is isolated, the entire curve corresponds to that single state, and only the state index is marked on the curve. For clarity, dashed lines are used to distinguish overlapping stable branches associated with different states. Black lines denote stable branches, and different shades of gray indicate unstable solutions with different numbers of negative eigenvalues (NE) of the Hessian matrix[Eq.(10)]. All subsequent figures follow the

*Contact author: jiaying.zhang@buaa.edu.cn

same plotting and notation conventions. To clearly illustrate the state transition of the system, Figs. 12(c)-(d) present the detailed transition pathways under forward loading, while Figs. 12(e)-(f) show the corresponding pathways under reverse loading.

Comparing the force–displacement responses and energy landscapes in Fig. 12 and Figs. 13(a)-(b) show that, even when all units share a consistent sequence of the maximum force F_{top} and minimum force F_{bot}, different relative positions of SN1, SN2, and the stable states in parameter space can still produce the same transition pathways. Comparing Fig. 12 and Figs. 13(c)-(d), in the former all state transitions are induced by SN1, whereas in the latter some transitions are induced by SN2. Since SN1 is related to the elastic connection of each unit, adding more units in series makes each unit effectively softer at its elastic connection, which promotes the formation of SN1. Figures 13(e)-(f) show that, when the ordering of the switching forces is inconsistent among the units, some stable states become unreachable; the same effect also appears in the two-unit system.

Figures 12 and 13 are simplified to transition graphs between states [5], as shown in Fig. 14. The three-unit system exhibits more complex pathways. However, under the assumptions that the avalanche length in the series system does not exceed 2 [5] and that each transition involves only one unstable unit [2], the system shows repeated features. In Fig. 14(d), enbolded states mark the involved units, and gray indicates units without transitions. This graph represents two repetitions of the two-unit diagram in Fig. 11(a). The two independent loops are linked via one-way paths corresponding to forward and backward loading.

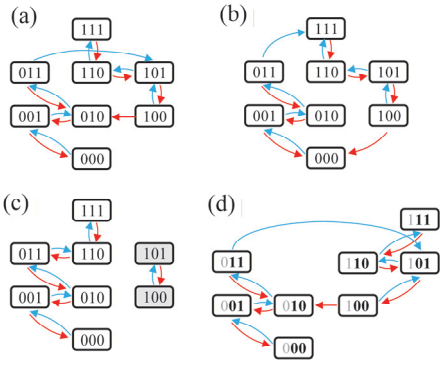

FIG 14. State transition graphs. This gives rise to recurring features, as shown in Fig. 11. (a) From Fig. 12 and Figs. 13(c)-(d), (b) from Figs. 13(a)-(b), (c) from Figs. 13(e)-(f). (d) recurring features.

Interestingly, Figs. 13(c)-(d) reveal additional stable branches beyond the eight states formed by the three units in different configurations. These branches are connected to unstable branches at both ends, so the system cannot reach this state through a single displacement-controlled loading.

TABLE II. The Data Used in Section V.D.

Set	K(BSU1/2/3/4)	α(BSU1/2/3/4)	β(BSU1/2/3/4)
1	0.12/0.03/0.025/0.01	1.0/1.8/2.1/3.5	2.0/3.6/4.2/7.0
2	0.005/0.01/0.015/0.02	2.0/2.0/2.0/2.0	4.0/4.0/4.0/4.0
3	0.12/0.04/0.02/0.01	1.2/1.9/3.0/4.0	2.0/3.6/4.5/7.0

D. Four-unit series system

Table II lists the series-unit data used in this section. Figures 15(a)-15(d) show the force–displacement responses and energy landscapes of the four-unit series systems. Even when all units follow the same force sequence, the relative positions of SN1 and the stable states in parameter space can produce identical transition pathways. In the four-unit series system, the connection stiffness of each unit is small, making SN2 less likely to occur. Figures 15(e)-15(f) show that when the switching force sequence of units becomes inconsistent, some stable states become inaccessible. Stable states are represented by the state vector $s = (s_4, s_3, s_2, s_1)$, where the subscript indicates the unit order.

Figures 15 is simplified into transition graphs between states, as shown in Fig. 16. Repeated two-unit features also appear in all state transition graphs. In Fig. 16(a), for the state sequence "0000–0001–0010–0011", units 3 and 4 remain unchanged, and the transition pathway matches the feature observed in the two-unit model. Such feature repetitions occur throughout all state transition graphs, connected via different pathways to form larger and more complex transition graphs.

E. *N*-unit series system

This section analyzes the force–displacement response of N units with identical characteristics. We focus on how increasing the number of units affects the occurrence of SN1, which depends on the connection stiffness. This model has been used in the analysis of discrete phase transformations [2] to explain the jagged force–displacement responses observed in systems ranging from proteins and sub-cellular components in biological systems to micro-scale structures of standard materials. However, the bifurcation mechanisms underlying these responses have not been clearly analyzed.

*Contact author: jiaying.zhang@buaa.edu.cn

.

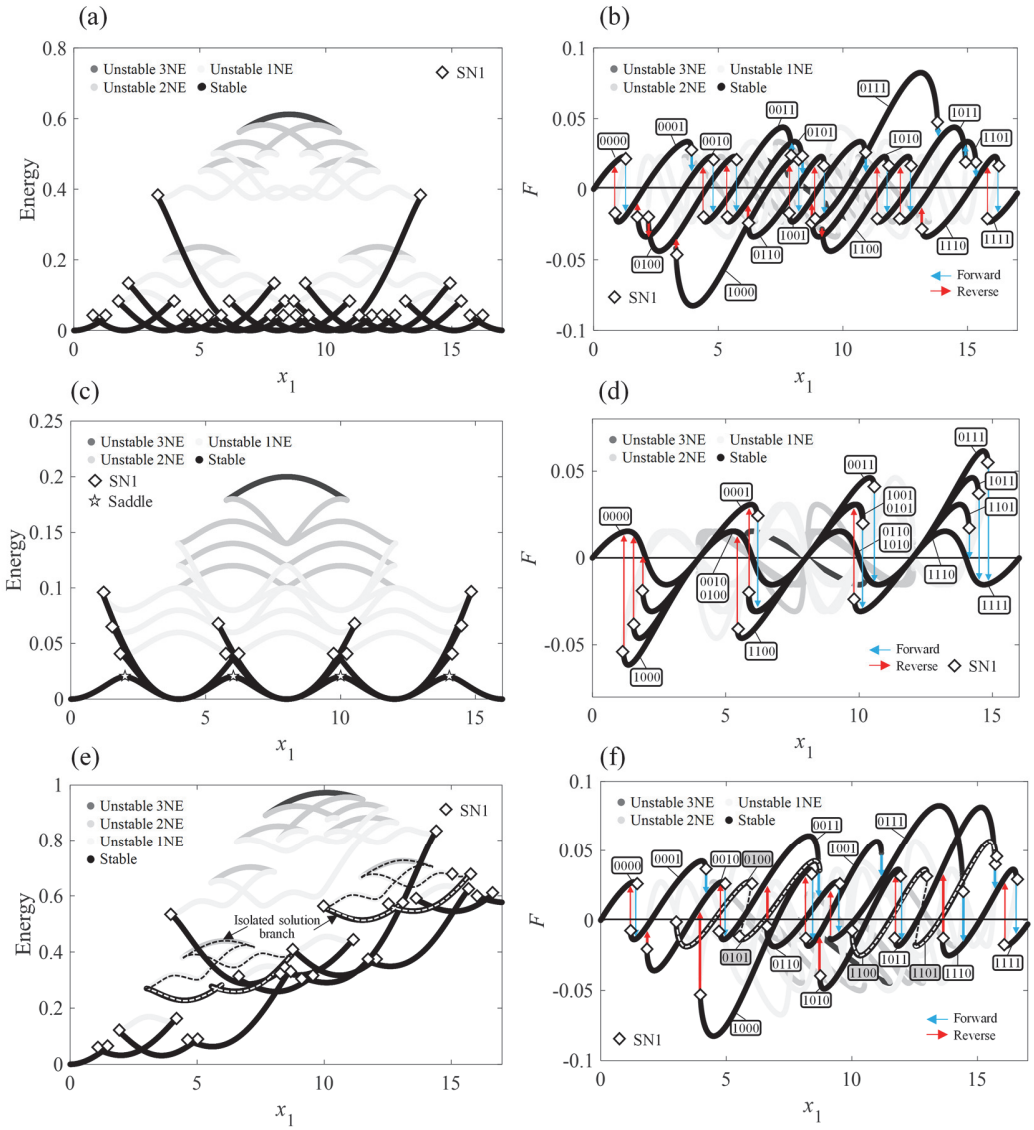

FIG. 15. Transition pathways of the four-unit series systems with parameter (a-b) set 5, (c-d) set 6, (e-f) set 7 in Table II. (a,c,e) Energy landscape, (b,d,f) Force–displacement relation. Gray shading indicates that the corresponding stable states become inaccessible.

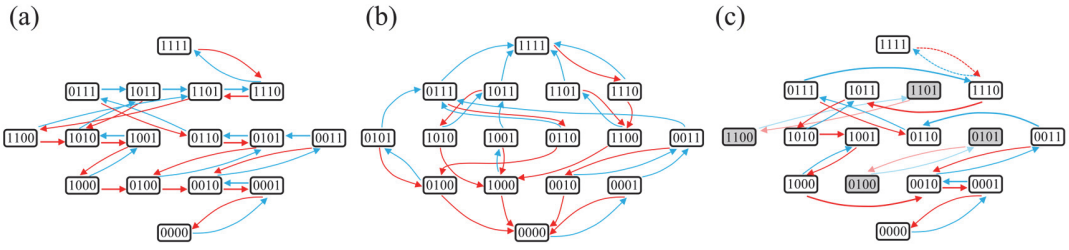

FIG. 16. State transition graphs of the four-unit series systems. (a) From Figs. 15(a) and (b), (b) from Figs. 15(c) and (d), (c) from Figs. 15(e) and (f). Gray shading indicates that the corresponding stable states become inaccessible.

Figure 17 shows the force–displacement responses for N units. When the number of units becomes large, unstable saddle points with higher Morse indices appear. For clarity, only the saddle points with a Morse

*Contact author: jiaying.zhang@buaa.edu.cn

index of 1 are shown in the figure, indicating that the Hessian matrix [Eq.(9)] of these stationary solutions has a single unstable eigenvalue. When the number of units is 2, SN1 and the associated snap-through do not appear. For more than 2 units, SN1 emerges, producing periodic snap-through. The force–displacement curve exhibits a jagged response, with the average force discontinuity of each snap-through decreasing as the number of units increases. This indicates that the macroscopic jagged response in more complex systems originates from periodic SN1 events in the microscopic units, with each discontinuity corresponding to the state transition of a single unit.

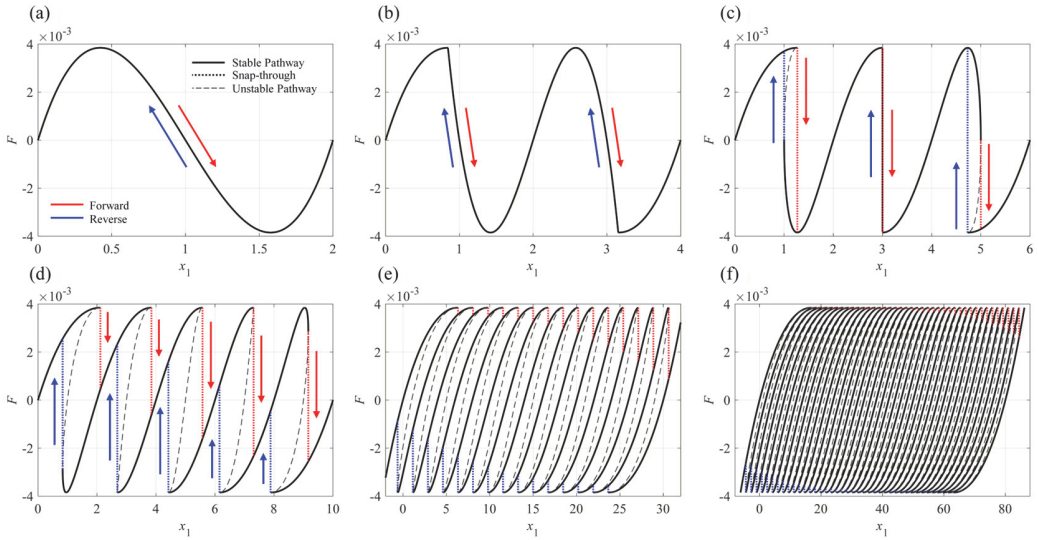

FIG. 17. Force–displacement responses of N-unit series systems. (a) Individual unit responses, (b) $N = 2$, (c) $N = 3$, (d) $N = 5$, (e) $N = 15$, (f) $N = 40$.

V. CONCLUSION AND OUTLOOK

We explored the potential energy landscape organized by bifurcation structures and the snap-through triggered by the annihilation of stable states due to SN bifurcations using theoretical, numerical, and experimental methods. Two types of elastic sequential snap-through instabilities are discovered. Adjusting the geometry and connection stiffness of units enables design of customized snap-through paths. As an application of the theoretical framework developed in this article, our recent work [38] employs multistable metamaterials composed of series-connected curved bi-stable beams to support the morphing skins of bio-inspired aircraft, whose state transitions enable smooth shape changes while maintaining load-bearing capacity.

This research method can be extended to more general bistable lattices, networks and continuous systems. For example, in 2D bistable lattices or 1D bistable chains with non-local effects [4, 39], where complex node competition occurs, equilibrium equations can be derived based on the degrees of freedom at connection nodes [18, 28, 29]. Flexible silicone viscoelasticity [37], along with the bottleneck effect [14], notably impact the dynamic response of complex multistable systems [35, 40]. Rather than approximating quasi-static loading by artificially increasing damping [40], our experimental framework achieves ideal quasi-static loading without external damping control, providing a powerful tool to probe the static energy landscape of multistable systems [16, 35, 40]. Future studies should examine bifurcation mechanisms in underdamped multistable systems including plates and shells to reveal complex dynamic behaviors.

ACKNOWLEDGMENTS

This project has received funding from National Natural Science Foundation of China (Grant No. 92271104, 12102017) and Beijing Natural Science Foundation (Grant No. 1232014).

Data availability——The data that support the findings of this article is openly avaliable [41]

*Contact author: jiaying.zhang@buaa.edu.cn

1. J. Yin, Y. Wang, J. Z. Y. Chen, et al., "Construction of a Pathway Map on a Complicated Energy Landscape," Phys. Rev. Lett. **124**, 090601 (2020).
2. G. Puglisi, L. Truskinovsky, "Mechanics of a discrete chain with bistable elements," J. Mech. Phys. Solids **48**, 1-27 (2000).
3. G. Puglisi, L. Truskinovsky, "Rate independent hysteresis in a bistable chain," J. Mech. Phys. Solids **50**(2), 165-187 (2002).
4. S. Nitecki, S. Givli, "The mechanical behavior of 2-D lattices with bistable springs," J. Mech. Phys. Solids **157**, 104634 (2021).
5. M. van Hecke, "Profusion of transition pathways for interacting hysterons," Phys. Rev. E **104**, 052604 (2021).
6. C. Findeisen, J. Hohe, M. Kadic, et al., "Characteristics of mechanical metamaterials based on buckling elements," J. Mech. Phys. Solids **102**, 151-164 (2017).
7. H. Mofatteh, B. Shahryari, A. Mirabolghasemi, et al., "Programming Multistable Metamaterials to Discover Latent Functionalities," Adv. Sci. **9**, e2202883 (2022).
8. N. C. Keim, J. D. Paulsen, Z. Zeravcic, et al., "Memory formation in matter," Rev. Mod. Phys. **91**(3), 035002 (2019).
9. A. Pal, M. Sitti, "Programmable mechanical devices through magnetically tunable bistable elements," Proc. Natl. Acad. Sci. U.S.A. **120**(15), e2212489120 (2023).
10. T. Mei, Z. Meng, K. Zhao, et al., "A mechanical metamaterial with reprogrammable logical functions," Nat. Commun. **12**(1), 7234 (2021).
11. J. Liu, M. Teunisse, G. Korovin, et al., "Controlled pathways and sequential information processing in serially coupled mechanical hysterons," Proc. Natl. Acad. Sci. U.S.A. **121**(22), e2308414121 (2024).
12. L. J. Kwakernaak, M. van Hecke, "Counting and Sequential Information Processing in Mechanical Metamaterials," Phys. Rev. Lett. **130**(26), 268204 (2023).
13. T. Yang, D. Hathcock, Y. Chen, et al., "Bifurcation instructed design of multistate machines," Proc. Natl. Acad. Sci. U.S.A. **120**(34), e2300081120 (2023).
14. M. Gomez, D. E. Moulton, D. Vella, "Critical slowing down in purely elastic 'snap-through' instabilities," Nat. Phys. **13**(2), 142-145 (2016).
15. B. Radisson, E. Kanso, "Elastic Snap-Through Instabilities Are Governed by Geometric Symmetries," Phys. Rev. Lett. **130**, 236102 (2023).
16. Q. Wang, A. Giudici, W. Huang, et al., "Transient Amplification of Broken Symmetry in Elastic Snap-Through," Phys. Rev. Lett. **132**(26), (2024).
17. I. Benichou, S. Givli, "Structures undergoing discrete phase transformation," J. Mech. Phys. Solids **61**(1), 94-113 (2013).
18. D. Shohat, D. Hexner, D. Lahini, "Memory from coupled instabilities in unfolded crumpled sheets," Proc. Natl. Acad. Sci. U.S.A. **119**(28), e2200028119 (2022).
19. S. Shan, S. H. Kang, J. R. Raney, et al., "Multistable Architected Materials for Trapping Elastic Strain Energy," Adv. Mater. **27**, 4296-4301 (2015).
20. A. Rafsanjani, A. Akbarzadeh, D. Pasini, "Snapping mechanical metamaterials under tension," Adv. Mater. **27**, 5931-5935 (2015).
21. A. S. Meeussen, M. van Hecke, "Multistable sheets with rewritable patterns for switchable shape-morphing," Nature **621**(7979), 516 (2023).
22. K. Bertoldi, V. Vitelli, J. Christensen, et al., "Flexible mechanical metamaterials," Nat. Rev. Mater. **2**, 17011 (2017).
23. S. H. Strogatz, *Nonlinear dynamics and Chaos: with applications to physics, biology, chemistry, and engineering*, Studies in Nonlinearity (Addison-Wesley Pub, 1994).
24. W. Huang, C. Ma, L. Qin, "Snap-through behaviors of a pre-deformed ribbon under midpoint loadings," Int. J. Solids Struct. **232**, (2021).
25. J. Qiu, J. H. Lang, A. H. Slocum, "A Curved-Beam Bistable Mechanism," J. Microelectromech. Syst. **13**, 137-146 (2004).
26. H. Hussein, P. Le Moal, R. Younes, et al., "On the design of a preshaped curved beam Bistable mechanism," Mech. Mach. Theory **131**, 204 (2019).
27. M. Vangbo, "An analytical analysis of a compressed Bistable buckled beam," Sens. Actuators A: Phys. **69**, 212 (1998).
28. D. Shohat and M. van Hecke, "Geometric Control and Memory in Networks of Hysteretic Elements," Phys. Rev. Lett., **134**, 188201 (2025).
29. M. Mungan, S. Sastry, K. Dahmen, and I. Regev, "Networks and Hierarchies: How Amorphous Materials Learn to Remember," Phys. Rev. Lett., **123**, 178002 (2019).
30. See Supplemental Material at [*URL will be*

*Contact author: jiaying.zhang@buaa.edu.cn

inserted by publisher] for further details of the analytical, numerical and experimental methods.
31. Y. S. Oh, S. Kota, "Synthesis of Multistable Equilibrium Compliant Mechanisms Using Combinations of Bistable Mechanisms," J. Mech. Des. **131**, 021010 (2009).
32. M. A. Ten Wolde, D. Farhadi, "A single-input state-switching building block harnessing internal instabilities," Mech. Mach. Theory 196, (2024).
33. R. Thom, *Structural stability and morphogenesis* (CRC Press, FL, 2018).
34. D. R. H. Borja, L. Truskinovsky. "Functionality of Disorder in Muscle Mechanics," Phys. Rev. Lett. **122**(8), 088103 (2023).
35. C. W. Lindeman, V. F. Hagh, C. I. Ip, et al., "Competition between Energy and Dynamics in Memory Formation," Phys. Rev. Lett. **130**(19), 197201 (2023).
36. R. M. Neville, R. M. J. Groh, A. Pirrera, et al., "Shape Control for Experimental Continuation," Phys. Rev. Lett. **120**, 254101 (2018).
37. M. Gomez, D. E. Moulton, D. Vella, "Dynamics of viscoelastic snap-through," J. Mech. Phys. Solids **124**, 781-813 (2019).
38. K. Huang, J. Zhang, C. Wang, Q. Wang, A. D. Shaw, and M. I. Friswell, "Mechanical Properties of Multistable Morphing Skin Structures with Large Deformation Capability," AIAA J. 63(12), 5226 - 5237 (2025).
39. Puglisi G, "Hysteresis in multistable lattices with non-local interactions," J. Mech. Phys. Solids **54**(10), 2060-2088 (2006).
40. L. Jin and M. van Hecke, "Dynamic Avalanches: Rate-Controlled Switching and Race Conditions," Phys. Rev. Lett. **135**, 218201 (2025).
41. K. Huang and J. Zhang, Data openly available at https://zenodo.org/records/17723895 (2025).

*Contact author: jiaying.zhang@buaa.edu.cn